Nonlinear continuous orbital-angular-momentum modulation of linearly polarized Bessel beams

Yue Chai,* Nicolas Marsal, and Delphine Wolfersberger
Université de Lorraine, CentraleSupélec, LMOPS, F-57000 Metz,France
and Chair in Photonics, CentraleSupélec, LMOPS, F-57070 Metz, France

(Received 5 December 2023; accepted 30 April 2024; published 15 May 2024)

We numerically and experimentally demonstrate the nonlinear continuous modulation of orbital angular momentum (OAM) of a linearly polarized high-order Bessel beam in a biased photorefractive (PR) crystal. According to the simulation results, we identify three nonlinear dynamic regimes depending on the strength of the applied electric field, and we successfully stabilize the OAM via the modulation of a background illumination. As a result, we predict a parabolic trend for the maximal OAM modulation range in the stable regime. In addition, with the comparative analysis between vortex and differently truncated Bessel beams, we report the existence of exploitable plateaus, enabling a more extensive modulation range in the unstable regime. The experimental results are consistent with the simulations, confirming the practical realization of the flexible control of the OAM in both stationary and dynamic regimes. These results contribute to new reconfigurable components in OAM-based communications.

DOI: 10.1103/PhysRevA.109.053518

I. INTRODUCTION

In recent years, orbital angular momentum (OAM) has attracted considerable attention because of its potential for classical and quantum information processing. The OAM carrying light presents a helical phase front described by $\exp(il\phi)$, where ϕ is the azimuthal angle, and l is the number of the 2π phase shift around the center of the beam phase profiles, which also indicates the mode of the OAM states. Different from spin angular momentum (SAM) associated with the circular polarization possessing only two modes ($s = \pm 1$), the OAM can take, in principle, unlimited orthogonal modes ($l = 0, \pm 1, \pm 2, ...$) [1,2]. Thus, as a new degree of freedom for encoding information, OAM-based spatial modes provide a higher traffic capacity in optical networks [3]. Meanwhile, as multilevel quantum states, OAM states permit higher transmission rates and security through a high-dimensional quantum key distribution (QKD) system in quantum communication [4–6].

For manipulating information encoded by the modes of the OAM states, the key challenge lies in their modulation. Thus, the OAM modulation of light beams becomes a current research interest for structured light [7]. Several technologies have been proposed, such as spiral phase plates [8], spatial light modulators [9], and metasurfaces [10]. While these approaches have seen significant innovation and advancements in recent years, they typically necessitate optical transformation before and following the modulation components, thereby introducing complexities in their practical realization. Moreover, they are always limited by nonreconfigurability and high costs. According to these challenges, we propose to realize the OAM modulation in an electro-optic crystal through phase modulation under nonlinear conditions. This method also takes full advantage of all-optical control, effectively addressing issues such as time delays and data distortions arising from the conversion between optical and electrical signals. Some research of the OAM modulation based on nonlinear effects has already been carried out recently. For example, in 2017, Mousavi *et al.* designed an integrated OAM states modulator due to the linear electro-optic effect in lithium niobate ($LiNbO_3$) [11]. This technology is based on the mathematical transformation of the Laguerre-Gauss (LG) modes to the Hermite-Gauss modes [12], so the modulator can only reverse the handedness of OAM states and is also limited by the type of the vortex beam. In 2020, Wu *et al.* realized the SAM-OAM conversion in a strontium-barium niobate (SBN) crystal [13]. It is restricted to an input beam circularly polarized with a propagation along the optical axis for a uniaxial condition. These results demonstrate the feasibility of OAM modulation under weak nonlinear conditions. Nevertheless, the research remains at the simulation stage, and the discussions do not concern the stability of the modulation. Moreover, the modulation in these works strictly requires the circular polarization state of the input beam, so the modulation value is limited to $\Delta l = 2$. In 2022, Jiang *et al.* experimentally realized the OAM conversion based on the sum frequency generation [14]. Despite an extensive range of modulation in this work, the modulated values are restricted to the integer domain, and the modulation requires a delicate choice of the pump beam.

Considering these limitations, it is intriguing to investigate (1) whether it is feasible to continuously modulate the OAM of a Bessel beam under nonlinear conditions, (2) whether the input polarization state is important for the OAM modulation, and (3) whether it is possible to realize such modulations in experiments. In this paper, we use high-order Bessel beams for conducting this research. The Bessel beam (BB) was proposed by Durnin in 1987 [15], and its Gaussian truncated form, the

*yue.chai@centralesupelec.fr

so-called Bessel-Gauss beam [16], has been widely studied in the last three decades. Due to their peculiar properties, such as nondiffraction [17,18], self-healing [19], and self-trapping behavior under the nonlinear propagating condition in the Kerr or photorefractive (PR) crystal [20], it is attractive for use in all-optical information processing, for example, the light localization by BB-inducing photonic lattice [21], the reconfigurable soliton network [22], and the photoinduction of complex wave-guiding structures [23–25]. In addition, high-order Bessel beams possess helical phase fronts and carry OAM depending on the orders of the Bessel function [26], which permits their use for classical optical and quantum communications [27–29]. Meanwhile, in this domain, high-order Bessel beams exhibit better robustness against turbulence and outperform other OAM-carrying beams, such as LG beams, in channel efficiency and bit error rates [30].

Accordingly, in this paper, contrary to other works, we inject a linearly polarized high-order BB in the PR SBN crystal, and study the electric field-modulated behavior of OAM. In the simulations, by analyzing the influence of the nonlinear conditions, we demonstrate the feasibility of such continuous OAM modulations through the applied electric field and identify three dynamic regimes of OAM variation depending on the strength of the applied electric fields: the stable state, the quasi-stable state with oscillations, and the unstable state. Then, by adjusting an optical parameter such as the background illumination in our crystal, we successfully determined the adapted intensity ratios to stabilize the OAM for each calculated external electric field and reported a parabolic modulating rule depending on the electric field. In addition, the comparison between the high-order Bessel beams and the vortex beam demonstrates the protection of the multirings profiles against the erratic and violent decline of the OAM under high nonlinear conditions. Subsequently, by discussing the beam truncation, we present the transient exploitable plateaus where the OAM is adjustable between the minimum stable value and a value higher than the original one, thereby expanding the modulation range. Finally, we conduct experiments and exhibit two stages of the OAM variation over time: the focusing and the relaxation stages. In both scenarios, we conclude the concordance between the experimental and simulation results, encompassing the OAM modulation tendency, three nonlinear dynamic regimes depending on the strength of the applied electric fields, and the extended modulation range under high nonlinear conditions. The simulations and experiments affirm the continuous OAM modulation of a linearly polarized high-order BB in both stable and unstable regimes with an extended range.

II. THEORY AND NUMERICAL MODEL

The typical scheme of a high-order Bessel beam propagating in a SBN crystal is illustrated in Fig. 1(a). As the OAM-carrying property is related to both intensity and phase characteristics, it is essential to calculate the propagation in the (2+1)D situation. We assume that the incident high-order Bessel beam is linearly polarized along the optical axis (c axis) of the SBN crystal [x axis in Fig. 1(a)] and propagates along the z axis (the crystal length is $L_0 = 2$ cm). This incident

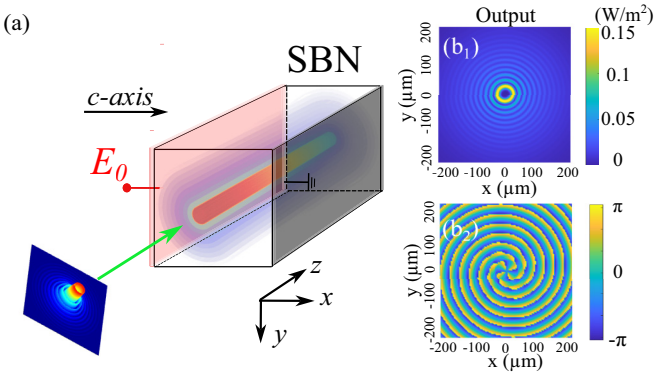

FIG. 1. (a) Principle scheme of a high-order Bessel beam illuminating a SBN crystal. (b_1 and b_2) Two-dimensional (2D) intensity and phase distributions at the output face of the crystal for a fourth-order Bessel beam ($l = 4$, $k_t = 0.2\,\mu\text{m}^{-1}$, $\omega_0 = 20r_0$, $I_{\text{in}}/I_d = 1$) linearly propagating in the 2-cm SBN crystal ($E_0 = 0\,\text{V/cm}$).

Bessel beam profile is mathematically defined by

$$F(r, \phi, z = 0) = F_0 J_l(k_t r) \exp\left(-\frac{r^2}{\omega_0^2}\right) \exp(il\phi). \quad (1)$$

$r = \sqrt{x^2 + y^2}$ and $\phi = \arctan(y/x)$ are the radial distance and the azimuthal angle, respectively, where (x, y) are transverse coordinates. F_0 is the maximum electric field amplitude of the incident beam related to the input intensity with $I_{\text{in}} = |F_0|^2$. J_l is the lth-order Bessel function, and k_t is the transverse wave number related to the beam size r_0 with $k_t = 2/r_0$. ω_0 is the waist of the Gaussian truncated beam, which determines the number of rings and the diffracting-free distance of the Bessel beam by $L_D = \omega_0/(k_t/k)$ ($k = 2\pi n/\lambda$ is the wave number in the crystal, $n = 2.3$ is the unperturbed refractive index of the SBN crystal, and $\lambda = 532$ nm is the wavelength of the beam) [23]. The phase term $\exp(il\phi)$ describes the helical wavefront of the high-order Bessel beam related to its OAM mode as mentioned in the Introduction.

When such a high-order Bessel beam propagates in the SBN crystal, as described by the Kukhtarev-Vinetskii model, the donors absorb the photons and ionize for the free electrons [31]. The ionized donors and the excited electrons move through diffusion and drift effect, which forms an internal field called the space charge field. With the same assumptions in Ref. [32,33], this process can be described by the normalized Kukhtarev-Vinetskii equations:

$$\tilde{N}_e = \frac{\xi(I + I_d)(\tilde{N_D} - \tilde{N_D^+})}{\tilde{N_D^+}}, \quad (2)$$

$$\tilde{N_D^+} = 1 + \tilde{\rho}, \quad (3)$$

$$\frac{\partial \tilde{\rho}}{\partial t} = -\nabla(\tilde{N}_e[\mu]\vec{E}) - \frac{k_B T}{e}\nabla([\mu]\nabla\tilde{N}_e). \quad (4)$$

$\tilde{N}_e$ is the free electron density normalized to the acceptor density N_A. $\tilde{N_D}$ and $\tilde{N_D^+}$ are total and empty donor densities normalized in the same way. $I(x, y, z)$ presents the light intensity distribution in the SBN crystal that varies over time in the nonlinear process. I_d is the intensity of the background illumination. $\tilde{\rho}$ is the space charge density normalized to eN_A, where

e is the elementary charge of an electron. ξ is the constant proportional to the ratio of the photoexcitation probability and the recombination probability. $[\mu]$ is the mobility tensor taking account of the anisotropy of the electron mobility in the SBN crystal. k_B and T are the Boltzmann constant and the absolute temperature, respectively.

$\vec{E}$ in Eq. (4) is the total electric field in the crystal, including the space charge field E_{sc} and the external electric field E_0. The space charge field E_{sc} can be calculated by the integration of the charge density distribution $\rho(\mathbf{r}')$ in the crystal volume V:

$$\vec{D}(\mathbf{r}) = \epsilon_0[\epsilon]\vec{E}_{sc}(\mathbf{r}) = \frac{1}{4\pi}\iiint_V \rho(\mathbf{r}')\frac{\mathbf{r}-\mathbf{r}'}{|\mathbf{r}-\mathbf{r}'|^3}\,d^3\mathbf{r}', \quad (5)$$

where ϵ_0 and $[\epsilon]$ are the vacuum permittivity and the relative permittivity in the material. With the same numerical method presented in Ref. [33], we calculate the space charge field for each time step Δt. This internal field induces a refractive index change through the Pockels effect, which can be determined by

$$\Delta\left(\frac{1}{n^2}\right)_{ij} = \sum_k r_{ijk}E_k, \quad (6)$$

where E_k are the electric field components and r_{ijk} are the linear electro-optic coefficients. With the novel refractive index change distribution Δn, the beam propagation can be described by the wave equation

$$i\partial_z F + \frac{1}{2k}\nabla^2 F + \frac{k}{n}\Delta n F = 0, \quad (7)$$

where F is the complex field of the light calculated concurrently by the beam propagation method (BPM) in each time step. In the following simulations, we set the total calculation duration to $5T_d$, where T_d is the relaxation time of the PR crystal [34]. This duration ensures the achievement of a stable state under weak nonlinear conditions, facilitating the following identification and analysis of the dynamic behaviors. Furthermore, to ensure consistency between simulations and experimental observations, all physical parameters of the SBN:61 crystal ($[\epsilon]$, $[\mu]$, n, r_{ijk}) [35,36] were taken into account in our simulations.

Then, according to Ref. [37], we can calculate the OAM distribution along the propagation axis (z axis) by the following definition:

$$l(z) = \frac{\iint\left(\frac{x\partial\psi}{\partial y} - \frac{y\partial\psi}{\partial x}\right)|F|^2\,dx\,dy}{\iint|F|^2\,dx\,dy}, \quad (8)$$

where ψ is the phase of the field F.

III. SIMULATION RESULTS

A. OAM modulation in the stationary regime

In the simulations, we first consider a fourth-order Bessel beam: $l = 4$, $k_t = 0.2\,\mu\text{m}^{-1}$, $\omega_0 = 20r_0$, $I_{in}/I_d = 1$ propagating linearly ($E_0 = 0\,\text{kV/cm}$) in an SBN crystal (2 cm) along the z axis.

Figures 1(b$_1$) and 1(b$_2$) show the 2D intensity and phase distributions at the back face of the crystal. As mentioned, we observe in Fig. 1(b$_1$) a dark region in the beam center

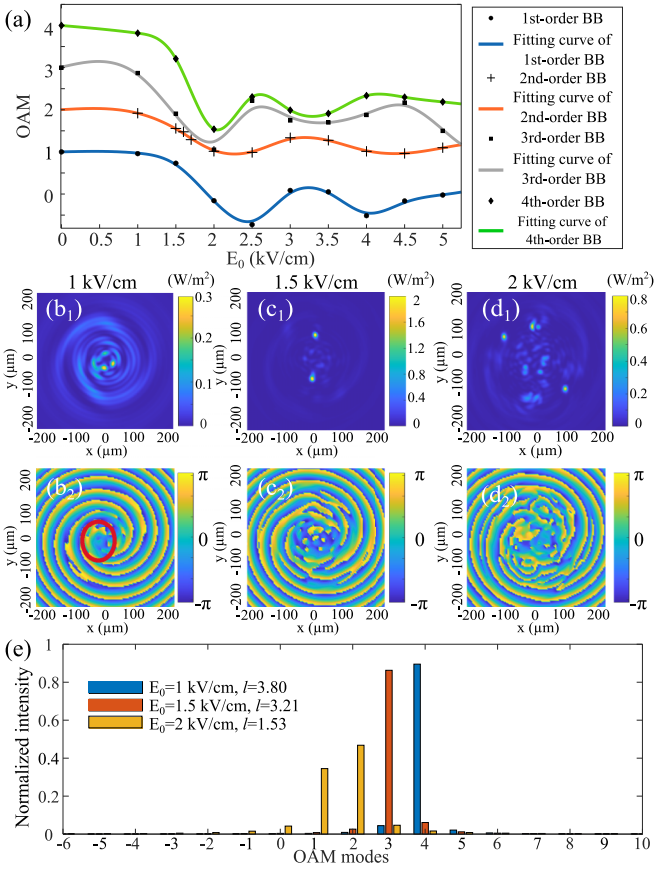

FIG. 2. (a) Variation tendency of the available OAM values versus electric field E_0 for the high-order Bessel beam ($l = 1, 2, 3, 4$) with $k_t = 0.2\,\mu\text{m}^{-1}$, $\omega_0 = 20r_0$, and $I_{in}/I_d = 1$ propagating in the 2-cm SBN crystal. (b$_1$–d$_2$) 2D output intensity and phase distributions of the fourth-order Bessel beam propagating under the condition of (b$_1$) and (b$_2$) $E_0 = 1\,\text{kV/cm}$, (c$_1$) and (c$_2$) $E_0 = 1.5\,\text{kV/cm}$, and (d$_1$) and (d$_2$) $E_0 = 2\,\text{kV/cm}$. (e) The OAM spectrum on the normalized intensity for the cases of $E_0 = 1\,\text{kV/cm}$, $E_0 = 1.5\,\text{kV/cm}$, $E_0 = 2\,\text{kV/cm}$.

characterizing the singularity of the OAM-carrying beam, and four 2π-phase shifts around the beam axis (z axis) indicating the beam order ($l = 4$) in Fig. 1(b$_2$). By calculating Eq. (8), we verify that such a Bessel beam maintains its OAM of $l = 4$ during its linear propagation in the SBN crystal.

Subsequently, we fix the intensity ratio of $I_{in}/I_d = 1$ of such a fourth-order Bessel beam and change only E_0 from $0\,\text{kV/cm}$ to $5\,\text{kV/cm}$ with a step of $0.5\,\text{kV/cm}$. For each E_0 value, we simulate its propagation for up to $5T_d$ and calculate the OAM value at the output face of the crystal ($z = L_0$) every $0.125T_d$. Then, we select the minimum OAM value during the $5T_d$ called the transient minimum in each case and plot them in Fig. 2(a) [the diamond points in Fig. 2(a)]. The green line is the fitting curve that depicts the tendency of these transient minimum OAM values that varies with electric field strength (E_0). Furthermore, we repeat the same process for other orders ($l = 1, 2, 3$) and plot the points representing the transient minimum OAM values with their fitting curves in Fig. 2(a). The coefficient of determination (R^2) for all these fitting curves is the same ($R^2 \approx 0.99$).

As depicted in Fig. 2(a), each curve exhibits a minimum at a specific $E_0 = E_{\min}$. For example, for the fourth-order Bessel beam [green line in Fig. 2(a)], the minimum is at $E_0 = 2\,\mathrm{kV/cm}$, where the exact minimum value is $l_{\min} \approx 1.53$, indicated by the diamond point. Notably, when $E_0 < E_{\min}$, the OAM value decreases in a monotonic way, indicating the potential for OAM modulation through the applied electric field E_0. This decreasing variation can be explained by the conversion of the OAM to SAM within the biased PR crystal, because the effective birefringence resulting from PR nonlinearity enables the transformation of linear polarization into elliptical polarization [38,39], also measured experimentally.

For more details, we present output intensity and phase distributions corresponding to the points at $E_0 = 1\,\mathrm{kV/cm}$, $E_0 = 1.5\,\mathrm{kV/cm}$, and $E_0 = 2\,\mathrm{kV/cm}$ in Figs. 2(b_1) and 2(b_2), 2(c_1) and 2(c_2), and 2(d_1) and 2(d_2), respectively. Figure 2(b_1) still shows a well-defined dark region at the center of the rotation pattern, while Figs. 2(c_1) and 2(d_1) show that the singularity distribution of the intensity becomes more noisy as E_0 increases. This phenomenon corresponds to the diminution of the OAM value. In addition, the phase distributions in Figs. 1(b_2) and 2(b_2)–2(d_2) reveal an increasing number of phase discontinuities emerging around the center of the beam as E_0 increases, for example, the phase step noted in the red circle in Fig. 2(b_2), which can be attributed to the self-phase modulation effect in a nonlinear PR crystal [40]. These phase discontinuities are consistent with the fractional OAM modes [41]. Moreover, as stated in Ref. [42], the spiral phase term of the high-order Bessel beam, $\exp(il\phi)$, can be represented using its Fourier series as $\exp(il\phi) = \sum_{-\infty}^{\infty} C_n(l)\exp(in\phi)$, where $|C_n(l)|^2 = I_n(l)$ denotes the intensity weight of the integer OAM state. Consequently, a beam featuring fractional OAM is defined as the decomposition into several integer OAM modes, each with their intensity weight $I_n(l)$. To specify the variation of intensity weights versus the electric field, we plotted the OAM spectrum on the normalized intensity $I_n(l)$ for the cases corresponding to Figs. 2(b_1)–2(d_2) in Fig. 2(e). The blue, orange, and yellow bars represent the intensity weight of the OAM states in the cases $E_0 = 1\,\mathrm{kV/cm}$, $E_0 = 1.5\,\mathrm{kV/cm}$, and $E_0 = 2\,\mathrm{kV/cm}$. Notably, the principal mode moves from $n = 4$ to $n = 1$ orders as the electric field strength increases, corresponding to the decrease in the average OAM value [the average OAM values calculated by Eq. (8) are 3.80 ($E_0 = 1\,\mathrm{kV/cm}$), 3.21 ($E_0 = 1.5\,\mathrm{kV/cm}$), and 1.53 ($E_0 = 2\,\mathrm{kV/cm}$), respectively]. Note that the modes are distributed more equally for $E_0 = 2\,\mathrm{kV/cm}$ because the decimal part of the average value approaches 0.5. Remarkably, as reported in Ref. [43], the fractional OAM modes enhance the robustness of OAM-based communications against atmospheric turbulence, which will be meaningful in optical communication. Furthermore, for the Bessel beam of other orders, due to the similar OAM variation tendencies versus E_0 shown in Fig. 2(a), we can also conclude the feasibility of the continuous OAM modulations under relatively weak electric fields ($E_0 < 2.5\,\mathrm{kV/cm}$ for the first-order Bessel beam, and $E_0 < 2\,\mathrm{kV/cm}$ for the second- and third-order Bessel beam, respectively).

So far, we have demonstrated the controllability of the OAM of a linearly polarized high-order Bessel beam through the applied electric field due to the linear electro-optic effect in a SBN crystal. In this way, we can potentially modulate the OAM of the first-order Bessel beam from $l = 1$ to $l' \approx -1$, the second-order Bessel beam from $l = 2$ to $l' = 1$, the third-order Bessel beam from $l = 3$ to $l' = 2$, and the fourth-order Bessel beam from $l = 4$ to $l' = 1.53$. Subsequently, an important aspect that warrants further investigation is the stability of the OAM. To address this concern, we take the case of the second-order Bessel beam as an example ($l = 2$, $k_t = 0.2\,\mu\mathrm{m}^{-1}$, $\omega_0 = 20r_0$, $I_{\mathrm{in}}/I_d = 1$) and individually plot the OAM variation curve in Fig. 3(a) [same as the orange line in Fig. 2(a)].

Depending on the temporal behavior of OAM under different electric fields, we identify three distinct nonlinear regimes in Fig. 3(a). The lightest shaded area on the left of Fig. 3(a) with the relatively weak electric field corresponds to the scenario where the OAM decreases monotonically versus time and finally achieves a value around which the fluctuations are less than 1% of their original OAM value. We define it as a stable state. For example, as denoted with a black frame in Fig. 3(b), at $E_0 = 1.6\,\mathrm{kV/cm}$, the OAM consistently decreases until $3.75T_d$ and then maintains the value around 1.49 with the fluctuations less than 0.02 ($\Delta < 0.02$). Then, as E_0 increases, the output OAM no longer monotonically decreases versus time. In the middle area in Fig. 3(a) ($2\,\mathrm{kV/cm} \leqslant E_0 < 3.5\,\mathrm{kV/cm}$), such as the case at $E_0 = 3\,\mathrm{kV/cm}$, as shown in Fig. 3(c), there is always a duration of $1T_d$ (in the black frame) where the OAM value oscillates around a certain value [about 1.6 in Fig. 3(c)], and the fluctuations are less than 15% of their original OAM value ($\Delta < 0.3$ for the second-order Bessel beam). Such phenomena with slight fluctuations in a duration longer than $1T_d$ are denoted quasi-stable states. To further clarify different dynamic states, we plot the intensity distributions at different moments indicated by the red triangles in Fig. 3(c) ($t = 1.25T_d$ [Fig. 3(c_1)], $t = 1.625T_d$ [Fig. 3(c_2)], and $t = 2.25T_d$ [Fig. 3(c_3)]). These figures are set with the same color bar scale. Upon comparing Fig. 3 with Figs. 3(c_1) and 3(c_2), we discern more localized spots in the center in Fig. 3(c_3), indicating a substantially more significant variation of the OAM in this case. This observation aligns with the fact that Figs. 3(c_1) and 3(c_2) correspond to the time interval characterized by minor perturbations, but Fig. 3(c_3) is situated out of this interval. Finally, when E_0 exceeds $3.5\,\mathrm{kV/cm}$, the temporal variation becomes completely irregular, the so-called unstable state, as the example with $E_0 = 4\,\mathrm{kV/cm}$ in Fig. 3(d).

The above discussion clarifies the temporal dynamic behaviors for different nonlinear regimes. It is essential to note that all analyses are only based on the output OAM states at $z = L_0 = 2\,\mathrm{cm}$. This observation raises the question of whether the identified nonlinear regimes resist when we change the propagation length. To address this question, we focus on the quasi-stable case in Fig. 3(c) and select several moments to plot the OAM variations along the propagation length in Fig. 3(c_4)). We observe that the OAM value decreases from $L = 0\,\mathrm{cm}$ to $L \leqslant 0.6\,\mathrm{cm}$ independently of the considering time. Above $L = 0.6\,\mathrm{cm}$, we can identify four types of dynamic behaviors referring to the spatiotemporal characteristics of the OAM:(1) the stable phase with only monotonic reduction ($t < 1T_d$), corresponding

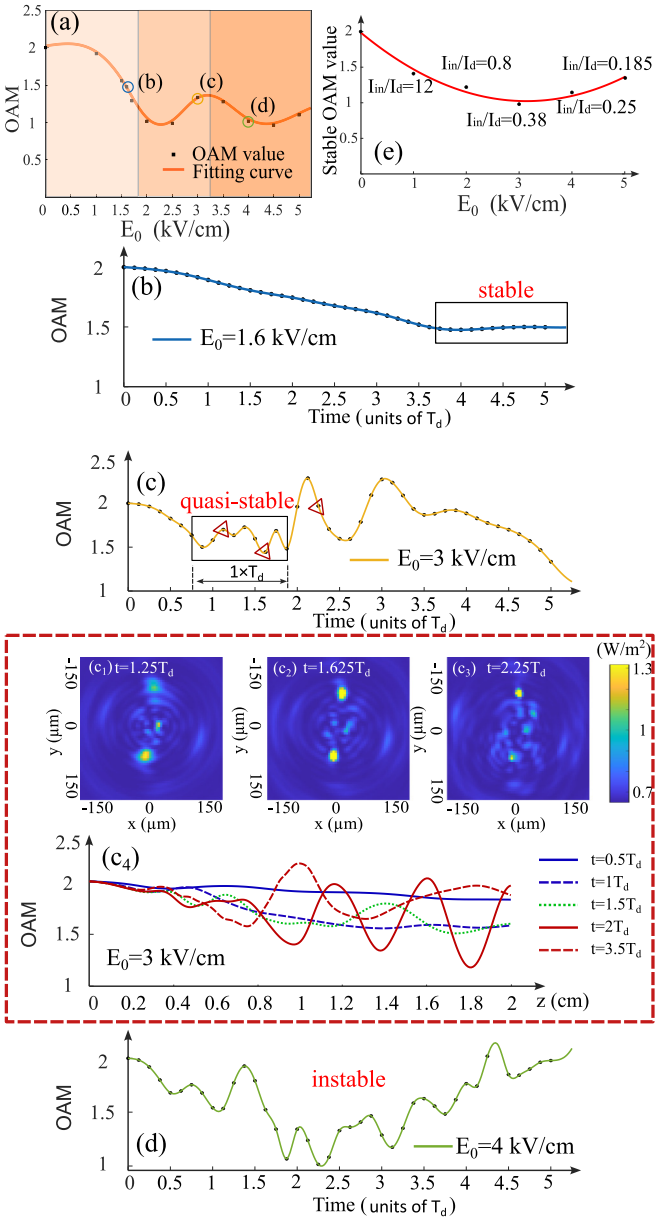

FIG. 3. (a) The variation of the output OAM versus the electric field E_0 for the second-order Bessel beam ($l = 2$, $k_t = 0.2\,\mu\text{m}^{-1}$, $\omega_0 = 20r_0$, $I_{\text{in}}/I_d = 1$) propagating in the 2-cm SBN crystal. (b–d) Temporal behavior of the output OAM at (b) $E_0 = 1.6\,\text{kV/cm}$, (c) $E_0 = 3\,\text{kV/cm}$, and (d) $E_0 = 4\,\text{kV/cm}$. (c_1–c_3) The intensity distribution at the moments (c_1) $t = 1.25T_d$, (c_2) $t = 1.625T_d$, and (c_3) $t = 2.25T_d$. (c_4) The OAM variation along the propagation length at different moments. (e) The achievable minimum stable OAM varying with the electric field and the intensity ratio.

to the time interval with monotonic evolution in Fig. 3(c); (2) the quasi-stable phase with slight oscillations ($1T_d < t < 2T_d$), coinciding with the time interval where the change in OAM value is less than 15% in Fig. 3(c); (3) the quasi-unstable phase with intense oscillations ($2T_d < t < 3.5T_d$); and (4) the unstable phase characterized by irregular variations ($t > 3.5T_d$). Importantly, these four stages correspond to the temporal variation of the OAM at $L = 2\,\text{cm}$ illustrated in Fig. 3(c), even though they are identified depending on the overall propagation behavior. Thus, the chosen output distances impact the final OAM value but not the identification of the three nonlinear regimes.

According to the above analysis, it is worth noting that the points depicted in Fig. 3(a), where $E_0 > 2\,\text{kV/cm}$, are all local minima in the temporal variation curves, which indicate the unstable states of the OAM. Even though it is possible to identify a quasi-stable state with a duration over $1T_d$ for $2\,\text{kV/cm} \leqslant E_0 < 3.5\,\text{kV/cm}$, the OAM value during that period ($l' \approx 1.5$) is close to the initial value ($l = 2$). This phenomenon implies a limited range of adjustment for the output OAM. Therefore, it is essential to stabilize the output OAM at a value significantly different from the initial one to break through this limitation. As we know, in a PR system with a Gaussian beam, the background intensity plays a significant role in the stability within the self-focusing and solitonic regime [44]. Thus, in the following, we investigate the influence of the background illumination I_d and try to stabilize the output OAM value to increase the parameter range where OAM is stable.

For each E_0, we fix the input intensity and change the background illumination to achieve different intensity ratios. When we find an intensity ratio value that permits the output OAM to reach its minimum in the stable state [similar to the case in Fig. 3(b)], we record the minimum value corresponding to the points in Fig. 3(e). We do the same calculation for E_0 from $1\,\text{kV/cm}$ to $5\,\text{kV/cm}$ with a step of $1\,\text{kV/cm}$. The red curve corresponds to a second-order polynomial fitting ($R^2 \approx 0.97$) for all the points. It is worth noting that the fitting curve exhibits the minimum [$l(E_0 = 3\,\text{kV/cm}) \approx 1$] at $E_0 = 3\,\text{kV/cm}$ with an intensity ratio of $I_{\text{in}}/I_d = 0.38$. This value indicates the maximum achievable range of OAM modulation within the stable regime. In addition, we notice a significant difference in the light intensity ratios among different cases (different E_0). Especially at $E_0 = 1\,\text{kV/cm}$, the output OAM achieves its stable minimum value at an intensity ratio of $I_{\text{in}}/I_d = 12$, approximately 30 times greater than that at $E_0 = 3\,\text{kV/cm}$. Compared to the OAM value indicated at $E_0 = 1\,\text{kV/cm}$ in Fig. 3(a) ($l' \approx 1.9$ with $I_{\text{in}}/I_d = 1$), the OAM value with the intensity ratio of $I_{\text{in}}/I_d = 12$ in Fig. 3(e) is much smaller ($l' \approx 1.4$). This observation implies that the high ratio $I_{\text{in}}/I_d = 12$ provides more free charges for the drift effect in the crystal so that the OAM can be changed more significantly due to a higher nonlinear effect. Even so, this OAM value is still much higher than the stable value at $E_0 = 3\,\text{kV/cm}$ shown in Fig. 3(e) because of the limitation imposed by the weak electric field. On the other hand, for higher electric field strengths, such as $E_0 = 5\,\text{kV/cm}$, the increased background illumination (lower intensity ratio) provides fewer free charges for the drift effect to achieve a stable state. In this case, the OAM modulation based on the nonlinear effect will be limited by the number of free charges in the crystal. Thus, the stable OAM values exhibit an upward trend beyond $E_0 = 3\,\text{kV/cm}$.

In summary, we can stabilize the output OAM values for any electric field strength with suitable background illuminations. Meanwhile, it is possible to identify a group of nonlinear parameters ($E_0 = 3\,\text{kV/cm}$, $I_{\text{in}}/I_d = 0.38$) to achieve the minimum OAM at the stable state, which indicates the maximum OAM modulation range in the stationary

regime. In addition, it is worth mentioning that although the above analysis is based on the second-order Bessel beam, the outcomes can be generalized to Bessel beams of any other order.

B. OAM modulation in the unstable regime

In the prior section, we demonstrated the feasibility for modulating the OAM of the light in a stationary regime by comprehensively adjusting the intensity ratio (I_{in}/I_d) and the electric field strength (E_0) in the biased PR crystal. This result paves the way for developing OAM-based communication components, for example, OAM-based modulators, switchers, and routers. As stated above, in the case of high electric field strengths, stabilizing the light OAM requires an ultra-low ratio between the input beam intensity and the background illumination ($I_{in}/I_d = 0.25$ for $E_0 = 4\,\mathrm{kV/cm}$ and $I_{in}/I_d = 0.185$ for $E_0 = 5\,\mathrm{kV/cm}$), which imposes practical challenges. Therefore, it is interesting to investigate the intrinsic characteristics of Bessel beams for stabilizing their OAM during the nonlinear propagation.

For this purpose, we begin with a comparative analysis between a high-order Bessel beam and an ordinary vortex beam, both possessing an OAM but the latter the simplest profile among all OAM-carrying beams. This time, we focus on the fourth-order Bessel beam because of its remarkable potential adjustment range ($\Delta_{OAM} \approx 2$), as shown in Fig. 2(a). Following the same method for plotting Fig. 2(a), we change the electric field strength (E_0) from $E_0 = 0\,\mathrm{kV/cm}$ to $E_0 = 5\,\mathrm{kV/cm}$ with a step of $1\,\mathrm{kV/cm}$. For each E_0, we simulate the propagation of a fourth-order vortex beam ($r_0 = 10\,\mu\mathrm{m}$) throughout $5T_d$. In each simulation, we calculate the OAM value at the output face of the crystal every $0.25T_d$ and select the minimum value within the whole simulation duration. Then, we plot these points and their fitting curve in Fig. 4(a). The blue line with the star points represents the OAM variation tendency for this fourth-order vortex beam, and the green line with the diamond points represents the fourth-order Bessel beam ($l = 4$, $k_t = 0.2\,\mu\mathrm{m}^{-1}$, $\omega_0 = 20r_0$, $I_{in}/I_d = 1$), which is the same as shown in Fig. 2(a) [also green line with the diamond points in Fig. 2(a)]. It is worth noting that when $E_0 < 3\,\mathrm{kV/cm}$, the OAM of the Bessel beam exhibits a faster rate of decrease at the beginning concerning E_0 and also possesses a broader potential adjustment range ($\Delta_{OAM} \approx 2$). As E_0 increases ($E_0 > 3\,\mathrm{kV/cm}$), the OAM value of the vortex beam declines rapidly to a negative value, whereas that of the Bessel beam remains almost constant at around 2.

For visual comparison, we present the intensity and phase distributions at the output face of the crystal at $E_0 = 5\,\mathrm{kV/cm}$. Figures 4(b_1) and 4(b_2) show the 2D output intensity and phase distributions for the vortex beam at $t = 4.75T_d$ corresponding to the star point plotted in Fig. 2(a) at $E_0 = 5\,\mathrm{kV/cm}$. Figures 4(c_1) and 4(c_2) present the 2D intensity and phase distributions for the Bessel beams at the moment $t = 3.625T_d$ corresponding to the diamond point plotted in Fig. 2(a) at $E_0 = 5\,\mathrm{kV/cm}$. As observed in Fig. 4(b_1), the energy appears dispersed in the case of the vortex beam, while in Fig. 4(c_1), the filament spots are all localized within the rings. Similarly, we notice that the phase dislocations of the vortex beam are also dispersed, as shown in Fig. 4(b_2),

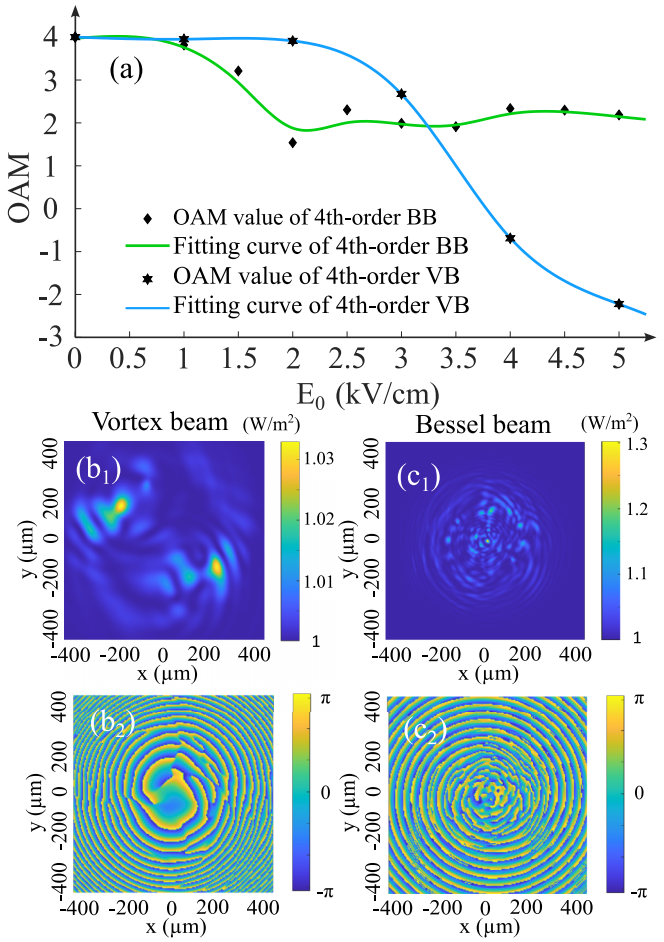

FIG. 4. (a) Variation tendencies of the output OAM versus electric field E_0 for the fourth-order Bessel beam with $k_t = 0.2\,\mu\mathrm{m}^{-1}$ and the fourth-order vortex beam with $r_0 = 10\,\mu\mathrm{m}$ propagating in the 2-cm SBN crystal. (b_1 and b_2) 2D output intensity and phase distributions of the fourth-order vortex beam at $E_0 = 5\,\mathrm{kV/cm}$ at the moment $t = 4.75T_d$. (c_1 and c_2) 2D output intensity and phase distributions of the fourth-order Bessel beam at $E_0 = 5\,\mathrm{kV/cm}$ at the moment $t = 3.625T_d$.

while those of the Bessel beam in Fig. 4(c_2) are concentrated around the center of the beam and surrounded by external rings. This phenomenon indicates that the multiring structure effectively protects the beam from dislocations under high nonlinear conditions, corroborating the results about LG beams mentioned in Ref. [45].

Then, to further specify the influence of the multiring structure on the OAM modulation of a Bessel beam, we consider the beam truncation characterized by the waist ω_0. For a more straightforward discussion, we introduce a parameter $a_t = 1/\omega_0$ to quantify the truncation strength. As discussed in Ref. [23], beam truncation determines the number and intensity distribution of the rings. In the following, we focus on the fourth-order vortex beam discussed in the last section and three fourth-order Bessel beams, respectively, with the truncation of $a_t = 1/\omega_0 = 1/7r_0$, $a_t = 1/\omega_0 = 1/10r_0$, and $a_t = 1/\omega_0 = 1/25r_0$. Figure 5(a) exhibits the one-dimensional profiles along the x axis of these fourth-order Bessel beams (green solid line for $a_t = 1/7r_0$, gray dashed line for $a_t =$

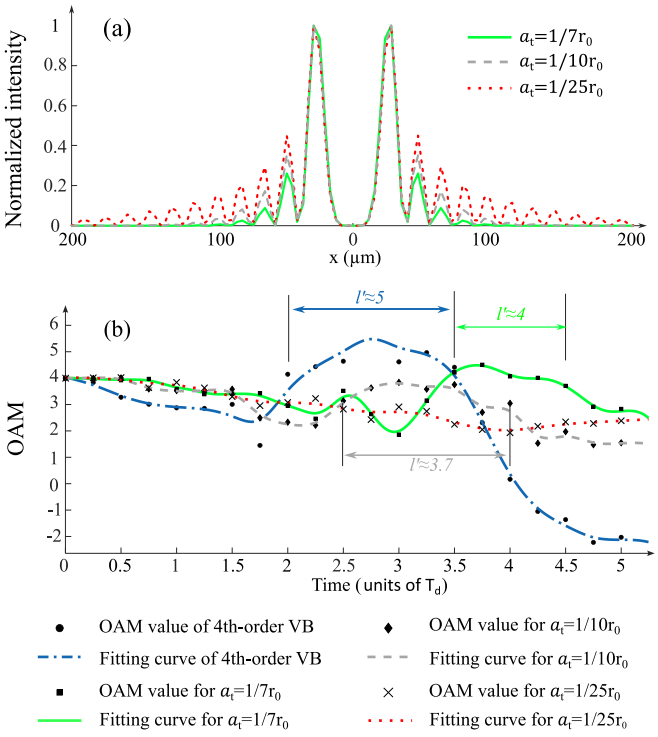

FIG. 5. (a) 1D intensity profiles of fourth-order Bessel beams truncated by the Gaussian term with $a_t = 1/7r_0$, $a_t = 1/10r_0$, and $a_t = 1/25r_0$ (normalized by their individual maximum intensities). (b) Temporal behaviors of the fourth-order vortex beam ($r_0 = 10\,\mu$m) and three fourth-order Bessel beams with the truncation parameter of $a_t = 1/7r_0$, $a_t = 1/10r_0$, and $a_t = 1/25r_0$ ($l = 4$, $k_t = 0.2\,\mu\text{m}^{-1}$) propagating in the 2-cm SBN crystal under the electric field of $E_0 = 5\,\text{kV/cm}$.

$1/10r_0$, red dotted line for $a_t = 1/25r_0$). Notably, as the truncation increases (a_t increases), there is a significant reduction in the number of external rings, accompanied by a weakening of their intensity ($a_t = 1/7r_0$).

To analyze the temporal behavior of multiring beam structures, we simulate their propagation under the electric field of $E_0 = 5\,\text{kV/cm}$ throughout the $5T_d$ period and calculate the OAM value at the output face of the crystal ($L_0 = 2\,\text{cm}$) in a time step of $0.25T_d$. We plot these points and their fitting curves in Fig. 5(b). The blue dash-dotted line (vortex beam), the green solid line (Bessel beam with $a_t = 1/7r_0$), and the gray dashed line (Bessel beam with $a_t = 1/10r_0$) all present a plateau of duration above $1T_d$ [$1.5T_d$ for the vortex beam ($t \in [2, 3.5]$) and the Bessel beam with $a_t = 1/10r_0$ ($t \in [2.5, 4]$), $1T_d$ for the Bessel beam with $a_t = 1/7r_0$ ($t \in [3.5, 4.5]$)], whereas, the red dotted line (Bessel beam with $a_t = 1/25r_0$) tends to be stable at the end of the calculation. This phenomenon implies that the multiring structure stabilizes the OAM of the light in a biased SBN crystal even under high nonlinearity. In addition, we notice that the OAM value of the plateau in the case of the higher truncated Bessel beam ($a_t = 1/7r_0$) is close to or even a little higher than the initial value ($l' \approx 4$), while the value for the Bessel beam with $\omega_0 = 10r_0$ ($l' \approx 3.7$) is smaller than the original one. Combined with the case of weakest truncation ($a_t = 1/25r_0$), we can conclude that it is possible to exploit a quasi-stable plateau with the OAM value controllable by the truncation parameter, so by the profile of the Bessel beam. Furthermore, as mentioned in Ref. [20], in the linear case, the external rings of the Bessel beam compensate for the diffraction of the internal structure, so the Bessel beam exhibits the diffracting-free property. This explanation implies the relation between the external rings' profiles and the Bessel beam diffraction. Accordingly, the occurrence of the OAM plateau can also be explained by the diffraction of the Bessel beam related to the truncation parameter, and the diffraction level can control the OAM level of the plateau. Thus, considering the limiting case without any external rings, i.e., the vortex beam, the most diffracted during the linear propagation, presents a time plateau with an OAM value ($l' \approx 5$) much greater than the initial value under the high nonlinear condition. This observation no longer obeys the angular momentum conservation law discussed in Ref. [13]. In our case, the beam propagates along the direction perpendicular to the c axis of the crystal, so the applied electric field, especially the high-strength field, can be considered as an external force onto the system to break the conservation of the total angular momentum. Thus, the OAM is generated despite using a linearly polarized beam (SAM = 0) with the intense nonlinear effect depending on the biased PR crystal. This phenomenon permits a broader modulation range through the beam truncation and a new function of using the PR effect for manipulating OAM.

IV. EXPERIMENTAL RESULTS

So far, our simulations have synthetically demonstrated that the OAM of a high-order BB can be modulated continuously in the PR crystal by the applied electric field. In the preceding discussion, by analyzing different conditions, including the background illumination and the beam truncation, we delimited the stability and the range of the OAM modulation. To confirm these simulation results and explore additional intriguing phenomena, using the identical setup detailed in Ref. [24], we conducted experiments for propagating the high-order BB in the biased PR crystal. By using a spatial light modulation (SLM), it is easy to change the order of the input beam by changing the number of discontinuities in the phase mask applied on the SLM. Furthermore, to correct the beam aberrations caused by the reflection angle of the SLM, we introduce an elliptic parameter to the phase mask, as explained in Ref. [46]. This procedure ensures that the deformations of the beams and the variations in OAM arise exclusively from the nonlinearity in the crystal.

Besides, to analyze the OAM of the output beam, referring to Eq. (8), it is necessary to retrieve the optical electric field, especially the phase distribution. Thus, according to Ref. [47], we introduce a second arm in the setup made of a plane wave to interfere with the output beam, employing off-axis digital holography to retrieve its electric field.

Figure 6(a) plots the experimental analysis of OAM temporal variations for a fourth-order BB propagating within the 1-cm SBN crystal used in Ref. [24]. We keep several beam parameters, including the beam power at 76 μW and the dark hole center diameter at 56 μm, corresponding to $k_t = 0.2\,\mu\text{m}^{-1}$. We systematically varied the applied electric field from 1 kV/cm to 6 kV/cm and recorded the interference

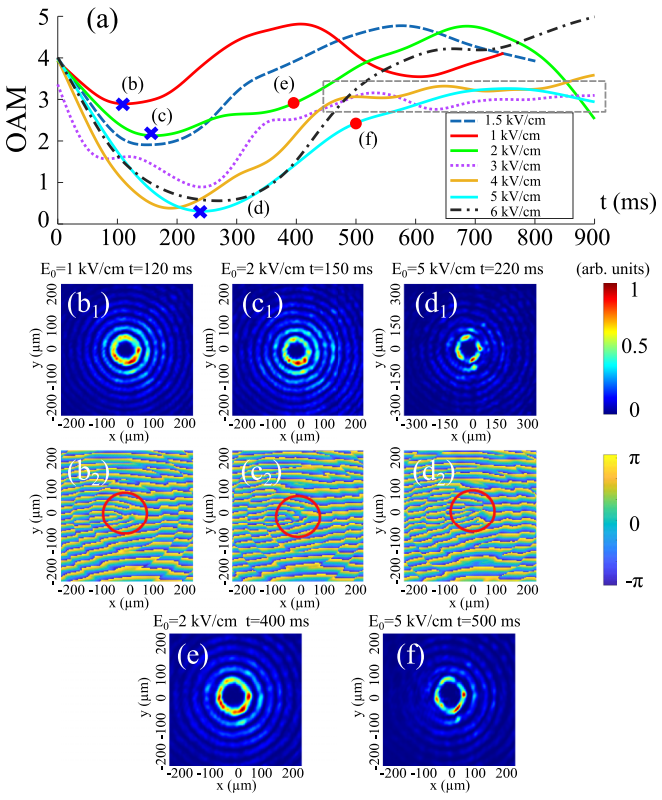

FIG. 6. (a) Temporal behaviors of the OAM measured in the experiments of the fourth-order BB propagates ($k_t = 0.2\,\mu\text{m}^{-1}$, $l = 4$) in the 1-cm SBN crystal under the nonlinear conditions with different strength of the electric field. (b_1–d_2) Intensity and phase distributions: (b_1) and (b_2) under $E_0 = 1\,\text{kV/cm}$ at $t = 120\,\text{ms}$, (c_1) and (c_2) under $E_0 = 2\,\text{kV/cm}$ at $t = 150\,\text{ms}$, and (d_1) and (d_2) under $E_0 = 5\,\text{kV/cm}$ at $t = 220\,\text{ms}$, corresponding to the blue crosses marked in (a). (e and f) Intensity distributions: (e) under $E_0 = 2\,\text{kV/cm}$ at $t = 400\,\text{ms}$ and (f) under $E_0 = 5\,\text{kV/cm}$ at $t = 500\,\text{ms}$, corresponding to the red dots marked in (a).

patterns with the time separation of $\Delta t \approx 25\,\text{ms}$ in each case. We retrieve the corresponding field through *off-axis digital holography* and calculate the OAM at each step by Eq. (8). Then, fitting curves, each representing a specific applied electric field, are depicted in distinctive colors, as indicated in the legend of Fig. 6(a).

It is worth noting that each curve can be outlined in two phases: the focusing stage, characterized by beam deformation and decreasing OAM, and the relaxation stage, during which the beam deformation restores with an upswing in OAM. For example, for the red curve ($E_0 = 1\,\text{kV/cm}$), the OAM value decreases before $t = 150\,\text{ms}$, referred to as the focusing stage, and after that, enters the relaxation stage with an increasing OAM.

Firstly, we focus on the focusing stage. Considering the minima in each case, the value decreases versus the strength of the electric field before $E_0 = 4\,\text{kV/cm}$ and nearly persists the same after 4 kV/cm. This variation tendency aligns qualitatively with the green curve in Fig. 2(a). The retrieved intensity and phase distributions corresponding to the cases $E_0 = 1\,\text{kV/cm}$ at $t = 120\,\text{ms}$, $E_0 = 2\,\text{kV/cm}$ at $t = 150\,\text{ms}$, and $E_0 = 5\,\text{kV/cm}$ at $t = 220\,\text{ms}$ are presented in Figs. 6(b_1)–6(d_2). As shown in Fig. 6(b_1), the center rings remain complete under $E_0 = 1\,\text{kV/cm}$, while under $E_0 = 5\,\text{kV/cm}$ shown in Fig. 6(d_1), they tend to split into four segments.

In addition, an increasing number of direct or inverse fork structures become apparent in the phase distributions with higher E_0, as indicated inside the red circles in Figs. 6(b_2)–6(d_2). All these observations indicate the progressively heightened deformation in both intensity and phase distributions as the applied electric field strengthens, consistent with the simulation results in Figs. 2(b_1)–2(d_2).

Secondly, for thorough clarification regarding the relaxation stage, we specify two cases identified by the red dots in Fig. 6(a): intensity distribution (1) under $E_0 = 2\,\text{kV/cm}$ at $t = 400\,\text{ms}$ in Fig. 6(e) and (2) under $E_0 = 5\,\text{kV/cm}$ at $t = 500\,\text{ms}$ in Fig. 6(f). Compared to the intensity distributions in the focusing stage [Figs. 6(c_1) and 6(d_1)], the center pattern in each case gradually relaxes, returning to circles resembling the initial state. We note that the rings under the high electric field, as shown in Fig. 6(f), are more compact and retain the splitting pattern, corresponding to the lower OAM value indicated in Fig. 6(a). Thus, similar to the focusing stage, in this regime, the intense applied electric field results in the decrease of the OAM, thereby suggesting conformity with the variation tendency in the simulation results in Fig. 2(a).

On the other hand, as we have stated three nonlinear regimes with the simulation results in Fig. 3, we can similarly identify three regimes depending on the relaxation behaviors observed in the experiments. The first regime, characterized by a relatively weak electric field ($E_0 \leqslant 2\,\text{kV/cm}$), corresponds to the red ($E_0 = 1\,\text{kV/cm}$), dark dashed blue ($E_0 = 1.5\,\text{kV/cm}$), and green curves ($E_0 = 2\,\text{kV/cm}$) in Fig. 6(a), where the OAM value returns to and oscillates around the initial value. The second regime, associated with the purple dotted ($E_0 = 3\,\text{kV/cm}$), yellow ($E_0 = 4\,\text{kV/cm}$), and bright blue ($E_0 = 5\,\text{kV/cm}$) curves, achieve a final value around 3, as indicated in the gray frame in Fig. 6(a). The last regime, involving the unstable state, refers to the case of $E_0 = 6\,\text{kV/cm}$, where the upswing of the OAM value is irregular, even reaching a much higher value than the initial, which can be explained by the discussion about the beam truncation denoted in Fig. 5.

These three nonlinear regimes also qualitatively conform to those described in Figs. 3(b)–3(d). Nevertheless, by comparing the simulation results [Fig. 5(b)] and the experimental results (Fig. 6), several quantitative disparities are observed, especially the exact OAM values. Firstly, our calculation, based on Eq. (4) for the temporal response of the crystal, is sensitive to the choice of the time step. In our simulations, we discretized "$5T_d$" into 1000 steps. This choice is sufficient to observe the OAM modulation and its dynamic behavior analysis while avoiding protracted computations due to computational constraints. Nevertheless, this choice may be insufficient for a precise theoretical value, potentially leading to inaccuracies. Additionally, as we calculate the OAM value at each 50-time step, there might be moments with lower values that are not accounted for in the calculations. Secondly, considering the experiments, several practical conditions contribute to these differences—for example, the low value of the background illumination. Besides, the phase extraction relies on off-axis digital holography. As the interference is

not always perfect in the transient regime, we unfortunately introduce phase errors.

Regardless, since these limitations and errors do not influence our qualitative analysis of the feasibility and the dynamic behavior of the OAM modulations, our experimental results are in agreement with the above simulation results. Furthermore, referring to Fig. 6(a), reaching nearly zero value in the focusing stage and surpassing the initial value in the relaxation regime both signify a notable expansion of the OAM modulation range under high nonlinear conditions, breaking the limitations in the previous works indicated in the introduction.

V. CONCLUSION

In conclusion, we numerically and experimentally demonstrated the continuous OAM modulation in a biased PR crystal by propagating a linearly polarized OAM-carrying beam under nonlinear conditions. Firstly, in the simulations, taking the second-order Bessel beam as an example, we analyzed its temporal behavior under different electric fields and identified three nonlinear dynamic regimes: stationary, quasi-stable, and unstable state. We confirm the possibility of stabilizing the light OAM for any electric field by adjusting the background illumination. In this way, we determined the nonlinear parameters (E_0 and I_{in}/I_d), which enable the minimum OAM value in the stationary state, i.e., the maximum stable OAM modulation range. The results are generalized for Bessel beams of any other orders. Subsequently, by comparing a vortex beam and different truncated Bessel beams, we demonstrated that under high nonlinear conditions, the multiring profiles of the Bessel beam protect its phase from dislocations and protect its OAM from dramatic and irregular variation. We exhibit the existence of an exploitable OAM plateau over $1T_d$ under high electric field conditions, proposing the OAM modulation in a broader range through the beam truncation control. Finally, the experimental results qualitatively present good agreement with the simulation analysis, involving the OAM variation tendency versus the electric field, three nonlinear dynamic regimes, and the extended OAM modulation range.

Furthermore, both numerical and experimental results confirm that the OAM modulation is achievable with a high-order Bessel beam in the linear polarization state despite the SAM being equal to 0. As indicated in Ref. [39], beam propagation exhibits a nonlinear phenomenon as long as the input light possesses a field component parallel to the c axis to activate the PR nonlinearity. Thus, the importance of the initial polarization state is whether the input beam includes such a field component for the focusing effect. For further research, it is interesting to investigate OAM modulation with a different polarized input Bessel beam.

Besides, it is worth mentioning that both numerical and experimental results are based on the average OAM values calculated by Eq. (8). Even though we have explored the intensity weight change versus the electric field, the discussion is insufficient for a rigorous quantitative demonstration. Further exploration is considered to directly extract the intensity weights from the output light field and investigate their modulation. For this research, many techniques are available, such as using the 2D multifocal array method outlined in Ref. [42], the interferometric method described in Ref. [48], and the Stokes fluctuations method denoted in Ref. [49]. This research also offers the potential to discover more intriguing phenomena for OAM communication applications.

All the results and discussions pave the way for designing new reconfigurable OAM modulators for optic or quantum communications. Furthermore, as we observe the OAM-generation phenomenon under the high electric field in both simulations and experiments, it is beneficial to study its temporal stability to exploit it for designing the OAM-generation components.

ACKNOWLEDGMENTS

We thank F. Devaux, V. Coda, and M. Chauvet for the development of the (2+1)D numerical model. This work is supported by the Chair in Photonics, Airbus GDI Simulation, Departement de la Moselle, European Regional Development Fund, CentraleSupelec, Fondation Supelec, and Metz Metropole, China Scholarship Council (CSC).

[1] L. Allen, M. W. Beijersbergen, R. J. C. Spreeuw, and J. P. Woerdman, Phys. Rev. A **45**, 8185 (1992).
[2] A. M. Yao and M. J. Padgett, Adv. Opt. Photon. **3**, 161 (2011).
[3] A. E. Willner, K. Pang, H. Song, K. Zou, and H. Zhou, Appl. Phys. Rev. **8**, 041312 (2021).
[4] M. Mafu, A. Dudley, S. Goyal, D. Giovannini, M. McLaren, M. J. Padgett, T. Konrad, F. Petruccione, N. Lütkenhaus, and A. Forbes, Phys. Rev. A **88**, 032305 (2013).
[5] M. Mirhosseini, O. S. Magaña-Loaiza, M. N. O'Sullivan, B. Rodenburg, M. Malik, M. P. Lavery, M. J. Padgett, D. J. Gauthier, and R. W. Boyd, New J. Phys. **17**, 033033 (2015).
[6] A. Sit, F. Bouchard, R. Fickler, J. Gagnon-Bischoff, H. Larocque, K. Heshami, D. Elser, C. Peuntinger, K. Günthner, B. Heim, C. Marquardt, G. Leuchs, R. W. Boyd, and E. Karimi, Optica **4**, 1006 (2017).
[7] Y. Shen, X. Wang, Z. Xie, C. Min, X. Fu, Q. Liu, M. Gong, and X. Yuan, Light Sci. Appl. **8**, 90 (2019).
[8] W. Harm, S. Bernet, M. Ritsch-Marte, I. Harder, and N. Lindlein, Opt. Express **23**, 413 (2015).
[9] J. Liu and J. Wang, Sci. Rep. **5**, 9959 (2015).
[10] I. Nape, B. Sephton, Y.-W. Huang, A. Vallés, C.-W. Qiu, A. Ambrosio, F. Capasso, and A. Forbes, APL Photonics **5**, 070802 (2020).
[11] S. F. Mousavi, R. Nouroozi, G. Vallone, and P. Villoresi, Sci. Rep. **7**, 3835 (2017).
[12] A. T. O'Neil and J. Courtial, Opt. Commun. **181**, 35 (2000).
[13] X. Wu, Y. Peng, H. Qiu, K. Chen, Y. Wu, D. Deng, and X. Yang, Opt. Express **28**, 24399 (2020).
[14] J.-Q. Jiang, H.-J. Wu, B.-S. Yu, C.-Y. Li, X.-Y. Zhang, X.-P. Hu, B.-S. Shi, and Z.-H. Zhu, J. Opt. **25**, 024004 (2023).
[15] J. Durnin, J. Opt. Soc. Am. A **4**, 651 (1987).

[16] F. Gori, G. Guattari, and C. Padovani, Opt. Commun. **64**, 491 (1987).
[17] D. McGloin and K. Dholakia, Contemp. Phys. **46**, 15 (2005).
[18] S. N. Khonina, N. L. Kazanskiy, S. V. Karpeev, and M. A. Butt, Micromachines **11**, 997 (2020).
[19] I. Litvin, L. Burger, and A. Forbes, J. Opt. **17**, 105614 (2015).
[20] M. Flammini, G. Di Domenico, D. Pierangeli, F. Di Mei, A. J. Agranat, and E. DelRe, Phys. Rev. A **98**, 033808 (2018).
[21] R. Fischer, D. N. Neshev, S. López-Aguayo, A. S. Desyatnikov, A. A. Sukhorukov, W. Krolikowski, and Y. S. Kivshar, J. Mater. Sci.: Mater. Electron. **18**, 277 (2007).
[22] Z. Xu, Y. V. Kartashov, and L. Torner, Opt. Express **13**, 1774 (2005).
[23] Y. Chai, N. Bouldja, N. Marsal, and D. Wolfersberger, Opt. Express **29**, 40231 (2021).
[24] Y. Chai, N. Marsal, and D. Wolfersberger, Phys. Rev. Appl. **17**, 064063 (2022).
[25] Y. Chai, N. Marsal, and D. Wolfersberger, Sci. Rep. **12**, 17566 (2022).
[26] K. Volke-Sepulveda, V. Garcés-Chávez, S. Chávez-Cerda, J. Arlt, and K. Dholakia, J. Opt. B: Quantum Semiclassical Opt. **4**, S82 (2002).
[27] N. Mphuthi, L. Gailele, I. Litvin, A. Dudley, R. Botha, and A. Forbes, Appl. Opt. **58**, 4258 (2019).
[28] K. S. Morgan, J. K. Miller, W. Li, Y. Li, and E. G. Johnson, in *OCEANS 2017 - Anchorage* (IEEE, New York, 2017), pp. 1–4.
[29] Y. Yuan, T. Lei, Z. Li, Y. Li, S. Gao, Z. Xie, and X. Yuan, Sci. Rep. **7**, 42276 (2017).
[30] T. Doster and A. T. Watnik, Appl. Opt. **55**, 10239 (2016).
[31] N. Kukhtarev, V. Markov, S. Odulov, M. Soskin, and V. Vinetskii, in *Landmark Papers On Photorefractive Nonlinear Optics* (World Scientific, Singapore, 1995), pp. 37–48.
[32] F. Devaux, V. Coda, M. Chauvet, and R. Passier, J. Opt. Soc. Am. B **25**, 1081 (2008).
[33] V. Coda, C. Ciret, T. Mengis, M. Gorram, G. Montemezzani, M. Chauvet, and F. Devaux, Opt. Commun. **355**, 382 (2015).
[34] P. Günter, J.-P. Huignard, and A. M. Glass, *Photorefractive Materials and Their Applications* (Springer, New York, 1988), Vol. 1.
[35] K. Buse, A. Gerwens, S. Wevering, and E. Krätzig, J. Opt. Soc. Am. B **15**, 1674 (1998).
[36] N. Korneev, D. Mayorga, S. Stepanov, A. Gerwens, K. Buse, and E. Krätzig, Opt. Commun. **146**, 215 (1998).
[37] F. Gori, M. Santarsiero, R. Borghi, and G. Guattari, Eur. J. Phys. **19**, 439 (1998).
[38] B. Crosignani, M. Segev, D. Engin, P. D. Porto, A. Yariv, and G. Salamo, J. Opt. Soc. Am. B **10**, 446 (1993).
[39] E. Fazio, W. Ramadan, A. Belardini, A. Bosco, M. Bertolotti, A. Petris, and V. Vlad, Phys. Rev. E **67**, 026611 (2003).
[40] B. Y. Zel'dovich, N. G. Kataevskii, N. D. Kundikova, and I. I. Naumova, Quantum Electron. **25**, 1125 (1995).
[41] H. Zhang, J. Zeng, X. Lu, Z. Wang, C. Zhao, and Y. Cai, Nanophotonics **11**, 241 (2022).
[42] D. Deng, M. Lin, Y. Li, and H. Zhao, Phys. Rev. Appl. **12**, 014048 (2019).
[43] Z. Xu, C. Gui, S. Li, J. Zhou, and J. Wang, in *Advanced Photonics for Communications* (Optica Publishing Group, Washington, DC, 2014), p. JT3A.1.
[44] Z. Chen, M. Segev, and D. N. Christodoulides, Rep. Prog. Phys. **75**, 086401 (2012).
[45] Q. Wang, M. R. Belić, D. Mihalache, L. Zeng, L. Zhang, and J. Lin, Phys. Rev. E **106**, 054214 (2022).
[46] H. Cheng, C. Xia, S. M. Kuebler, and X. Yu, Opt. Commun. **475**, 126213 (2020).
[47] M. Lovisetto, Modélisation et observation expérimentale du mixing et de la relaxation violente dans un système gravitationnel analogue, Ph.D. thesis, Université Côte d'Azur, 2022.
[48] A. D'Errico, R. D'Amelio, B. Piccirillo, F. Cardano, and L. Marrucci, Optica **4**, 1350 (2017).
[49] T. Sarkar, R. Parvin, M. M. Brundavanam, and R. K. Singh, Opt. Lasers Eng. **155**, 107065 (2022).